



## Two-phase flow dynamics in a micro hydrophilic channel: A theoretical and experimental study



Sung Chan Cho, Yun Wang\*

Renewable Energy Resources Lab (RERL), Department of Mechanical and Aerospace Engineering, The University of California, Irvine, CA 92697-3975, USA

### ARTICLE INFO

#### Article history:

Received 5 April 2013

Received in revised form 12 September 2013

Accepted 1 November 2013

#### Keywords:

Micro channel  
Experiment  
Modeling  
Multiphase flow  
Flow pattern

### ABSTRACT

In this paper, two-phase flow dynamics in a micro hydrophilic channel are experimentally and theoretically investigated. Flow patterns of annulus, wavy, and slug are observed in the range of operating condition. A set of empirical models based on the Lockhart–Martinelli parameter and a two-fluid model using several correlations of the relative permeability are adopted; and their predictions are compared with experimental data. It shows that for low liquid flow rates most model predictions show acceptable agreement with experimental data, while in the regime of high liquid flow rate only a few of them exhibit a good match. Correlation optimization is conducted for individual flow pattern. Through theoretical analysis of flows in a circular and 2-D channel, respectively, we obtain correlations close to the experimental observation. Real-time pressure measurement shows that different flow patterns yield different pressure evolutions.

© 2013 Elsevier Ltd. All rights reserved.

### 1. Introduction

Micro-channels are widely used in modern engineering, such as lab-on-chips, PEM (Polymer Electrolyte Membrane) fuel cells, micro-heat pipes, and heat exchangers [1]. In PEM fuel cells, gas flow channels are characterized by their cross-section dimension at micro/millimeter scale and a length scale of around 10 cm [2]. In micro heat pipes, flow channels with 10~500  $\mu\text{m}$  hydraulic diameter are frequently used for cooling microelectronic chips or electronic devices thanks to their high heat conductance and large capability of heat transfer [3]. Micro-channel heat exchangers (MCHX) of hydraulic diameter ranging from 25  $\mu\text{m}$  to 5~6 mm are widely applied to HVAC systems [4,5]. Fig. 1 shows the channel system of PEM fuel cells or micro heat exchangers. Two-phase flows are frequently encountered in these devices as a result of water production or phase change. Because of micro-scale flow, surface tension is usually significant, as opposed to the gravitational or inertial forces, for the occasions of small Bond number ( $Bo = \rho g L^2 / \gamma$ ) or Capillary number ( $Ca = \mu U_G / \gamma$ ) [6]. In PEM fuel cells, liquid water can block the pathway of air flow and hamper oxygen supply for the electrochemical reactions [7]. In micro heat pipes, liquid-phase working fluid, driven by capillary force, may encounter a large resistance to the evaporator side, leading to dry out of the evaporator [3].

Flow pattern and pressure drop are two important characteristics of multiphase flow in micro channels. To visualize flow pattern,

transparent devices are usually designed [8–10]. Cheng et al. [11] reviewed various two-phase flow patterns. As the gas flow rate increases two-phase flow experiences bubbly flow, plug flow, churn flow, annular flow and mist flow. The type of flow patterns depend on the channel orientation (vertical/horizontal), surface tension, and contact angle. In micro channels, mist flow, droplet formation, annulus, and slug flow are frequently observed [12–14]. Lately, Neutron radiography is adopted to detect the in situ volume fraction of liquid water [15–18], revealing spatial and temporal variations of liquid water.

To characterize two-phase flow, pressure drop is frequently measured. David et al. [19] developed the correlation between pressure drop and heat flux in MCHXs both numerically and experimentally, and they found flow pattern affects both pressure drop and heat transfer coefficient. Zhang et al. [20] presented the pressure fluctuation in a MCHX with a channel cross-section around 10~200  $\mu\text{m}$ . They showed that bubble production greatly impacts the pressure. Wu and Cheng [21] studied the pressure drop in boiling instability analysis of MCHXs, and tested eight parallel micro channels under various mass and heat fluxes. Two-phase pressure oscillates when boiling becomes unstable.

Modeling is important to the study of two-phase flow fundamentals. The homogeneous flow assumption is often adopted in modeling, which uses average quantities as major variables regardless flow patterns. [22–23] Various empirical correlations using the Lockhart–Martinelli parameter, following the Martinelli method [24], have been proposed to validate experimental data [25–29]. Physics-based two-fluid models can be developed, which consists

\* Corresponding author. Tel.: +1 949 824 6004; fax: +1 949 824 8585.  
E-mail address: [yunw@uci.edu](mailto:yunw@uci.edu) (Y. Wang).

## Nomenclature

$A$	area [m <sup>2</sup> ]	$X$	Lockhart–Martinelli parameter [–]
$C$	Chisholm parameter [–]	<i>Greek letters</i>	
$D_h$	hydraulic diameter [m]	$\alpha$	charge transfer coefficient [–]
$f$	fanning friction factor [–]	$\gamma$	surface tension [N/m]
$F$	Faraday constant [96,485 C/mol]	$\xi$	Stoichiometric number [–]
$g$	gravitational acceleration [m/s <sup>2</sup> ]	$\mu$	viscosity [kg/m s]
$H$	channel height or tube diameter [m, mm]	$\rho$	density [kg/m <sup>3</sup> ]
$I$	current density [A/cm <sup>2</sup> ]	$\Phi^2$	two-phase friction multiplier [–]
$k$	relative permeability [–]	<i>Subscripts</i>	
$K$	absolute permeability [m <sup>2</sup> ]	$2\phi$	two-phase
$L$	channel length [m]	$c$	critical
$m$	mass flux [kg/s]	$C$	cathode
$n$	number of electrons transferred in the reaction [–]	$e$	effective
$p$	pressure [pa]	$G$	gas phase
$R$	gas constant [J/K mol]	$L, l$	liquid phase
$RH$	relative humidity [–]	$mem$	membrane
$s$	saturation [–]	$w$	water
$T$	temperature [K, °C]		
$U, u$	velocity [m/s]		
$W$	channel width [m]		
$Re$	Reynolds number [–]		
$x$	vapor quality [–]		

of two sets of governing equations to describe individual flow of the two phases. In porous media or capillary tubes, fluid flows can be described by Darcy's law. The relative permeabilities are usually defined to account for phase interaction [30–35]. Table 1 summarizes several empirical models using the Lockhart–Martinelli parameter and correlations for the relative permeability. In this work, flow pattern, two-phase friction multiplier, and real-time pressure drop are visualized/measured and presented under various conditions in a hydrophilic channels. Model predictions are compared with experimental data.

## 2. Experimental

### 2.1. Experimental setup

A single straight rectangular channel ( $1.68 \times 1.00 \times 150 \text{ mm}^3$ ) was designed and fabricated for experiment. Micro channels were

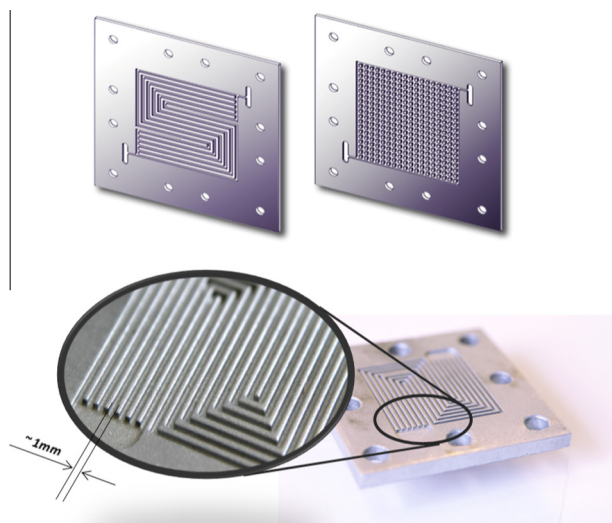


Fig. 1. Micro channels in PEM fuel cells or micro heat exchangers.

fabricated in a hydrophilic plate of 1.00 mm thickness using a high-precision CNC machine. The plastic components of the testing device were machined using the laser facility (precision: 50  $\mu\text{m}$ ) of the RapidTech on UCI campus. Fig. 2 shows schematic of the experimental test section. The machined channel plate of 1 mm thickness and the transparent window (polycarbonate) of 5.0 mm thickness are clamped between a base and an aluminum endplate with O-rings in between to seal the device. Micro holes were machined in the base plate and proper fittings were added for liquid water injection and air supply as well as pressure measurement. Humidified air ( $RH$  100%) is supplied by a mass flow controller, whereas liquid water is injected by a microfluidic pump with accuracy ( $\pm 0.35\%$ ,  $\pm 5.83 \times 10^{-10} \text{ m}^3/\text{s}$ ). The total channel length is 150 mm; and the distance for pressure drop measurement is 130 mm, which excludes the inlet and outlet areas (5 mm after the liquid injection site, and 10 mm ahead of the outlet). As the testing portion is away from the injection inlet and outlet ports, any unexpected disturbances arising from the presence of the inlet or outlet are diminished. In past, we observed two-phase flow in these areas caused local flow instability and liquid accumulation [30]. A camera-integrated microscope was placed over the transparent window to record flow pattern. The pressure drop was measured by a pressure transducer (Setra Model 230) with accuracy of  $\pm 0.25\%$  FS. A NI DAQ system (6025E & SCB100) was linked to the pressure transducer to record the data at a frequency of 10 Hz. In experiment, various flow conditions were investigated, with each condition repeated twice during the day (i.e. without restarting the test) and more than twice in different days (i.e. restart the testing). Fig. 3 shows the schematics of experimental setup.

### 2.2. Experimental procedure and method

Real-time pressure drop was measured in duration of up to 30 min. The camera records the real-time flow pattern in the last five minutes. Under high air flow rates, two-phase flow is stable with small fluctuation demanding short recording duration. Under low air flow rates, slug formation causes significant periodic fluctuation in pressure drop, thus it takes longer for measurement. In experiment, both single- and two-phase flows were tested for a

**Table 1**  
Two-phase pressure correlations and models.

Type	Author	Equation	Channel dimensions & working fluids
Empirical models	Lockhard and Martinelli [24]	$C = 5$	1.49–25.83 mm air; water, oil, hydrocarbons
	Mishima and Hibiki [25]	$C_{rec} = 21[1 - \exp(-0.319Dh)]$ $C_{cir} = 21[1 - \exp(-0.333D)]$	1.05–4.08 mm air; water
	Sun and Mishima [26]	$C = 1.79 \left(\frac{Re_G}{Re_L}\right)^{0.4} \left(\frac{1-x}{x}\right)^{0.5}$	0.506–12 mm air; water, refrigerant, CO <sub>2</sub>
	Li and Wu [27]	$C = 11.9Bo^{0.45} \quad Bo \leq 1.5$ $C = 109.4(BoRe_L^{0.5})^{-0.56} \quad (1.5 < Bo \leq 11)$	0.148–3.25 mm 12 fluids
	Zhang et al. [28]	$C = 21[1 - \exp(-0.674/Lo^*)]$ (liquid–gas) $C = 21[1 - \exp(-0.142/Lo^*)]$ (liquid–vapor)	0.07–6.25 mm 7 fluids
	Kim and Mudawar [29]	$C = 3.5 \times 10^{-5} Re_L^{0.44} Su_G^{0.50} \left(\frac{\mu}{\rho C}\right)^{0.48}$	0.0695–6.22 mm 17 fluids
Two-fluid model	Wang [30]	$k_{rL} = s_e^{n_k}, k_{rG} = (1 - s_e)^{n_k}$	1.0 mm air; water (theoretical)
	Nowamooz et al. [31]	$k_{rL} = s_e^{1.15}, k_{rG} = (1 - s_e)^{3.05}$	0.429 mm (Fracture) air; water
	Corey [40]	$k_{rL} = s_e^4, k_{rG} = (1 - s_e)^2(1 - s_e^2)$	Not specified gas; oil
	Fourar and Lenormand [33]	$k_{rL} = \frac{s_e^2}{2}(3 - s_i)$ , $k_{rG} = (1 - s_i)^3 + \frac{3}{2} \frac{\mu_G}{\mu_L} s_i(1 - s_i)(2 - s_i)$	Viscous coupling model
	Huang et al. [34]	$k_{rL} = \frac{s_e^2}{2}(3 - s_i)$ , $k_{rG} = (1 - s_i) \left[ \frac{3}{2} \frac{\mu_G}{\mu_L} + (1 - s_i)^2 \left(1 - \frac{3}{2} \frac{\mu_G}{\mu_L}\right) \right]$	Analytic modeling based on LBM
	Chen et al. [35]	$k_{rL} = 0.2677s_i^3 + 0.331s_i^2 + 0.3835s_i$ $k_{rG} = 0.502(1 - s_i)^3 + 0.1129(1 - s_i)^2 + 0.3483(1 - s_i)$	0.13 mm (Fracture) air; water

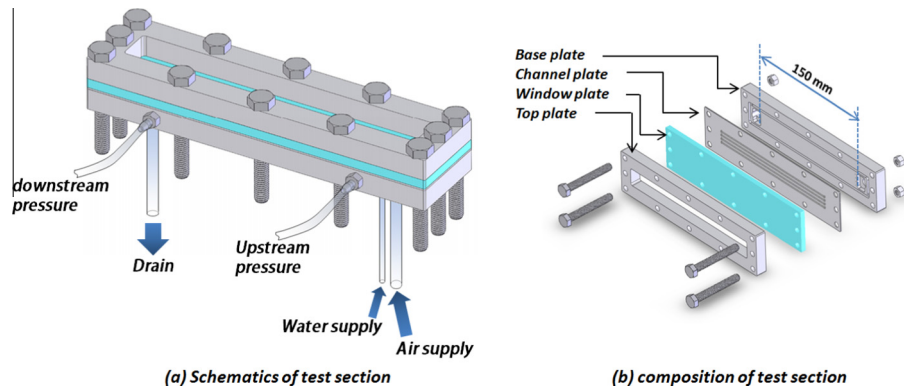


**Fig. 2.** Schematics of the experimental test device.

given air flow rate to measure the pressure drop and flow patterns. The specific experimental procedure is listed as follow:

- (1) Under no liquid injection, the flow is essentially single-phase flow: the single-phase pressure drop is measured at various air flow rates using the pressure transducer.
- (2) Liquid water is injected at a fixed rate with the air flow rate increasing from the lowest to highest velocity. Measurements are taken.
- (3) The liquid water rate is increased to another rate, with air velocity increasing from the lowest to highest velocity. Measurements are taken for each case.
- (4) Repeat (3) till the highest liquid flow rate is reached, then reduce the liquid flow rate and repeat the testing.
- (5) The testing is repeated in another day, and randomly set a liquid injection rate for measurement at various air flow rates.

Once the real-time pressure drop was obtained, the average pressure drop was calculated over all the data in the last five minutes of each run. The two-phase friction multiplier is calculated as

$$\Phi_G^2 = \frac{(dp/dx)_{two-phase}}{(dp/dx)_{single-phase}} \quad (1)$$

The uncertainty in the pressure amplifier measurement is calculated through the follow:

$$\delta\Phi_G^2 = \left\{ \left[ \frac{\Delta p_{two-phase}}{(\Delta p_{single-phase})^2} \cdot \delta\Delta p_{single-phase} \right]^2 + \left[ \frac{1}{\Delta p_{single-phase}} \cdot \delta\Delta p_{two-phase} \right]^2 \right\}^{1/2} \quad (2)$$

where  $\Delta p_{two-phase}$  and  $\Delta p_{single-phase}$  are the average measured pressure drops for two-phase and single-phase flows, respectively; and  $\delta\Delta p$  is obtained from the pressure transducer accuracy ( $\pm 0.25\%$  FS). Sample estimation of uncertainty is shown in Fig. 5.

### 2.3. Operating condition

In experiment, the operating condition of PEM fuel cells is used as reference: the water production rate is calculated via Faraday's law:

$$S_w = \frac{I \cdot A_{mem}}{2F} = \frac{I \cdot L \cdot W}{2F} \quad (3)$$

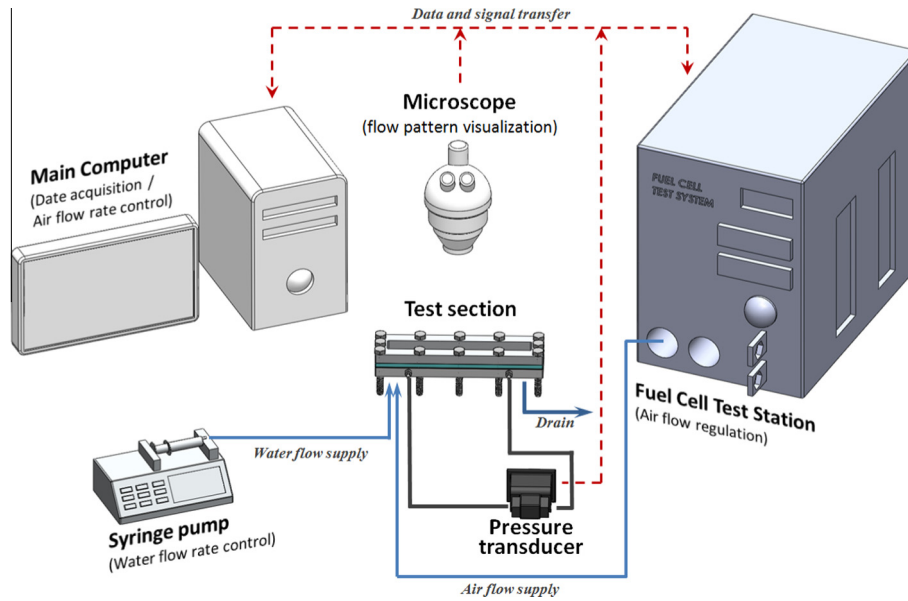


Fig. 3. Schematics of experimental setup.

where  $I$  is the current density,  $F$  is the Faraday's constant,  $A_{mem}$  is the membrane area for electrochemical reaction, and  $L$  and  $W$  are the length and width of a gas flow channel. With the water production rate, for same channel and land width the superficial velocity of liquid water at the channel outlet is calculated by:

$$U_L = \frac{I \cdot L \cdot M_w}{F \cdot \rho_w \cdot H} = \frac{M_w}{\rho_w} \frac{I \cdot L}{F \cdot H} \quad (4)$$

where  $H$  is the channel height. The channel air stream provides oxygen for the electrochemical reaction in PEM fuel cells. The superficial gas-phase velocity is calculated through the cathode flow stoichiometry  $\xi_c$  and current density  $I$ :

$$U_G = \frac{I}{4F} \frac{1}{C_{O_2}} \frac{L \cdot W}{0.5W \cdot H} \cdot \xi_c = \frac{1}{2C_{O_2}} \cdot \xi_c \cdot \frac{I \cdot L}{F \cdot H} \quad (5)$$

Thus, the ratio of the two superficial velocities gives:

$$\frac{U_G}{U_L} = \frac{\rho_w}{2C_{O_2} M_w} \cdot \xi_c \quad (6)$$

For a specific condition given below:

$$\frac{U_G}{U_L} = 2771.177 \cdot \xi_c \quad \text{for } 25^\circ\text{C}@1 \text{ atm} \quad (7)$$

$$\frac{U_G}{U_L} = 2073.146 \cdot \xi_c \quad \text{for } 80^\circ\text{C}@2 \text{ atm} \quad (8)$$

For the standard values of  $\xi_c$  in PEM fuel cells, e.g., 1.5 or 2.0, the gas-phase velocity is about 3000–4000 times higher than the liquid one, clearly indicating the sluggish liquid-phase flow. Fig. 4 presents the ratio between the air and water superficial velocities for typical operating conditions in PEM fuel cells. Experiment was conducted under room temperature; and the water and air flow rates are in the range of  $0.5 \times 10^{-4} \leq U_L \leq 1.0 \times 10^{-3}$  m/s and  $0.55 \leq U_G \leq 9.36$  m/s, respectively, i.e.  $0.39 \leq G_{gas}/G_{total} \leq 0.99$ .

### 3. Two-phase flow modeling

Numerous empirical and analytic two-phase models have been developed. A popular approach is to assume homogeneous properties of two-phase flow [22–23]. Empirical correlations using the Lockhart–Martinelli parameter, following the Martinelli method

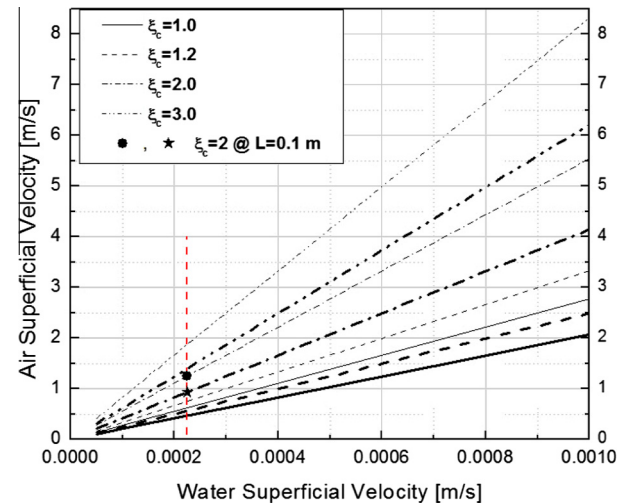


Fig. 4. Superficial phase velocities under various stoichiometry ratios ( $\xi_c$ ); and typical fuel cell operating condition ( $I = 1.0 \text{ A/cm}^2$ ) (thin line: 1 atm, 25 °C; thick line: 2 atm, 80 °C. channel cross section:  $1.0 \times 1.68 \text{ mm}^2$ ).

[24], have been proposed based on experimental data [25–29]. The two-fluid model is formulated with the governing equations developed for individual phase flows. In porous media or capillary tubes, the momentum equations of two phases can be approximated using Darcy's law with the relative permeabilities defined to account for phase interaction [30,31–35].

#### 3.1. Homogeneous flow model

Homogeneous flow models assume the mixture of two phases as a single phase fluid. The single-phase pressure relations are usually extended to two-phase flow using the average properties of the two-phase mixture:

$$\left(\frac{\Delta p}{\Delta z}\right) = 2f \frac{1}{D_h} \frac{G^2}{\rho_{2\phi}} \quad (9)$$

where  $f$  is the fanning friction factor,  $G$  is the mass flux of the two-phase flow, and  $D_h$  is the channel hydraulic diameter. The friction

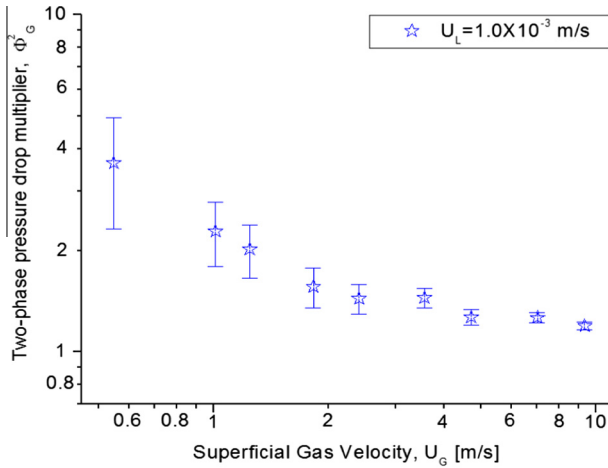


Fig. 5. Experimental uncertainty.

factor is determined by the Reynolds number. Several correlations of two-phase viscosity and density are suggested. McAdams et al. [22] gave:

$$\frac{1}{\mu} = \frac{x}{\mu_v} + \frac{1-x}{\mu_l} \quad (10)$$

The above is also suggested by Bittle and Pate [36] as the best match for flow in adiabatic capillary tubes for R134a, R22 and R152a. Another popular model is given by Cicchitti et al. [23] as

$$\mu = x\mu_v + (1-x)\mu_l \quad (11)$$

Beattie and Whalley [37] took into account flow pattern. For many bubble and annular flows, the two-phase viscosity is given by:

$$\mu = \mu_l(1 + 2.5\beta) \quad \text{for bubble flow} \quad (12)$$

$$\mu = \mu_l(1 - \beta) + \mu_v\beta \quad \text{for annular flow} \quad (13)$$

$$\text{where } \beta = \frac{\rho_l x}{\rho_l x + \rho_v(1-x)}$$

These homogeneous correlations are usually developed based on macro-scale pipe flows or high flow rates in which the capillary force and surface tension are less important.

### 3.2. Lockhart–Martinelli parameter and empirical models

The famous and widely applied correlation was developed by Lockhart and Martinelli [24]. They defined the Lockhart–Martinelli parameter ( $X$ ) and developed an empirical model based on the experiment results of flow of water, oils and hydrocarbons in 1.49–25.83 mm diameter pipes. The two-phase frictional multiplier ( $\Phi_G^2$ ) is defined to indicate the influence of two-phase flow on pressure drop, expressed as a function of the Lockhart–Martinelli parameter:

$$\Phi_G^2 = 1 + C \cdot X + X^2 \quad (14)$$

$$X = \frac{m_L}{m_G} \sqrt{\frac{\rho_G}{\rho_L}} \quad (15)$$

where  $C$  is the Chisholm parameter, a coefficient relevant to whether the flow is laminar or turbulent. For laminar liquid and gas flows, the value of  $C$  is 5. In addition to the base correlation provided by Lockhart and Martinelli, several empirical models were proposed for the coefficient. Mishima and Hibiki [25] proposed

the following coefficient  $C$  for air–water flow in rectangular and circular channels with a hydraulic diameter of 1.05–4.08 mm:

$$C = 21[1 - \exp(-0.319D_h)] \quad \text{for rectangular channel} \quad (16)$$

$$C = 21[1 - \exp(-0.333D)] \quad \text{for circular tube} \quad (17)$$

where  $D_h$  is the hydraulic diameter. Sun and Mishima [26] proposed another model by taking the ratio of the Reynolds numbers and mass quality  $x$  into account. The correlation is based on the experimental data of channels with a hydraulic diameter of 0.506–12 mm:

$$C = 1.79 \left( \frac{Re_G}{Re_L} \right)^{0.4} \left( \frac{1-x}{x} \right)^{0.5} \quad (18)$$

Li and Wu [27] compared experimental data and correlation models in previous literature, indicating that the Bond number and Reynolds number affect the coefficient  $C$ . Through statistical analysis, they showed that the correlation changes its form at  $Bo = 1.5$ :

$$C = 11.9Bo^{0.45} \quad \text{for } Bo \leq 1.5 \quad (19)$$

$$C = 109.4(BoRe_L^{0.5})^{-0.56} \quad \text{for } 1.5 < Bo \leq 11 \quad (20)$$

The database was obtained for a channel dimension of 0.148–3.25 mm and 12 fluids. Zhang et al. [28] obtained a general correlation of the Chisholm parameter based on previous experimental data. Following artificial neural network technique, a non-dimensional Laplace constant  $Lo^*$  is introduced ( $Lo^* \equiv [\gamma/g(\rho_L - \rho_G)]^{0.5}/D_h$ ):

$$C = 21[1 - \exp(-0.674/Lo^*)] \quad \text{for liquid–gas flow} \quad (21)$$

$$C = 21[1 - \exp(-0.142/Lo^*)] \quad \text{for liquid–vapor flow} \quad (22)$$

They pointed out that the mass flux, mass quality, and pressure have minor impact on the results. Kim and Mudawar [29] proposed a universal model based on about 7000 data and 17 fluids, and the hydraulic diameter ranging 0.0695–6.22 mm. They used the Suratman number, defined as  $Su = \rho\gamma D_h/\mu^2$ . For laminar liquid and gas flows, the Chisholm parameter  $C$  is correlated as:

$$C = 3.5 \times 10^{-5} Re_L^{0.44} Su_G^{0.50} \left( \frac{\rho_L}{\rho_G} \right)^{0.48} \quad (23)$$

where  $Re_L$  is the liquid-phase Reynolds number ( $Re_L = GD_h/\mu_L$ ) and  $Su_G$  is the gas-only Suratman number.

### 3.3. Two-fluid model

Two-fluid modeling is based on physics of fluid flows, consisting of two sets of governing equations for liquid and gas flows, respectively. In Wang [30], micro flow channels are treated as the pore network of a structured porous medium, thus Darcy's law is applicable. Applying Darcy's law to individual phase yields:

$$U_L = -\frac{k_{rL}K}{\mu_L} \frac{dP_L}{dx} \quad \text{for liquid phase} \quad (24)$$

$$U_G = -\frac{k_{rG}K}{\mu_G} \frac{dP_G}{dx} \quad \text{for gas phase} \quad (25)$$

where  $U_L$  and  $U_G$  denote the superficial velocities of liquid and gas phases, respectively, and  $k_{rL}$  and  $k_{rG}$  are the relative permeabilities, respectively. In PEM fuel cells, inlet dry air stream initially absorbs water from the ORR's production, till reaching its saturated state. When liquid emerges, all product water is added to liquid phase. Before that, the channel stream is essentially single phase flow. The transition point is denoted by  $x^*$ , then the pressure in the gas flow channel is given by [30]:

$$P_L = P_G(\bar{x}^*) - L_x \int_{\bar{x}^*}^x \frac{\mu_L U_L}{k_{rL} K} d\bar{x} \quad \text{for liquid phase} \quad (26)$$

$$P_G = P_G(\bar{x}^*) - L_x \int_{\bar{x}^*}^x \frac{\mu_G U_G}{k_{rG} K} d\bar{x} \quad \text{for gas phase} \quad (27)$$

A dimensionless pressure drop, scaled by the single-phase pressure, can then be derived as [30]:

$$\Delta \bar{P}_G = \bar{x}^* + \int_{\bar{x}^*}^1 \frac{1}{k_{rG}} d\bar{x} \quad (28)$$

Eq. (28) shows that the two-phase friction multiplier is a function of the gas-phase relative permeability. The relative permeability measures the interaction between the two phases, and is a function of the saturation. The following correlation is frequently used [30]:

$$k_{rL} = s_e^{n_k}, \quad k_{rG} = (1 - s_e)^{n_k} \quad (29)$$

where  $s_e$  is the effective liquid-phase saturation, given by:

$$s_e = [s_l - s_{ir}] / [1 - s_{ir}] \quad (30)$$

The value of  $n_k$  is usually set to be around 3~4 for the GDLs (Gas Diffusion Layers) of PEM fuel cells [38,39]. Several other correlations have been developed for the relative permeability. Nowamooz et al. [31] reported the optimized value of  $n_k$  as 1.15 and 3.05 for  $k_{rL}$  and  $k_{rG}$ , respectively. Corey [40] suggested  $n_k$  to be 4 for  $k_{rL}$ :

$$k_{rL} = s_e^4, \quad k_{rG} = (1 - s_e)^2 (1 - s_e^2) \quad (31)$$

Fourar and Lenormand [33] proposed a correlation taking into account the viscosities. They considered stratified flows between parallel plates. Through the Stoke's equation, viscous coupling is derived; and through generalized Darcy's equation the relative permeability is derived as below:

$$k_{rL} = \frac{s_l^2}{2} (3 - s_l), \quad k_{rG} = (1 - s_l)^3 + \frac{3}{2} \frac{\mu_G}{\mu_L} s_l (1 - s_l) (2 - s_l) \quad (32)$$

Similarly, Huang et al. [34] analytically derived the relative permeability for annulus in a 2-D channel:

$$k_{rL} = \frac{s_l^2}{2} (3 - s_l), \quad k_{rG} = (1 - s_l) \left[ \frac{3}{2} \frac{\mu_G}{\mu_L} + (1 - s_l)^2 \left( 1 - \frac{3}{2} \frac{\mu_G}{\mu_L} \right) \right] \quad (33)$$

Chen et al. [35] studied two-phase flow characteristics in fracture media. The dimension of fracture gap was ~0.13 mm and the working fluids are air and liquid water. They took a tortuous channel approach and fit the relative permeability with their experimental data:

$$k_{rL} = 0.2677s_l^3 + 0.331s_l^2 + 0.3835s_l \quad (34)$$

$$k_{rG} = 0.502(1 - s_l)^3 + 0.1129(1 - s_l)^2 + 0.3483(1 - s_l) \quad (35)$$

Table 1 summarizes a set of the two-phase correlations using the Lockhart–Martinelli parameter and relative-permeability correlations in two-fluid models.

### 3.4. Two-fluid model prediction under experiment condition

In experiments, the flow rates of air and liquid water are fixed under each operating condition. The air flow is fully humidified before fed into the channel. Assuming no supersaturated vapor state, the air and liquid flow rates are constant for the portion of channels where the pressure drop is measured, i.e. the distance of the transition point  $x^*$  is zero in the experiment. Then, Eq. (28) changes to:

$$\Delta \bar{P}_G = \frac{1}{k_{rG}} \quad (36)$$

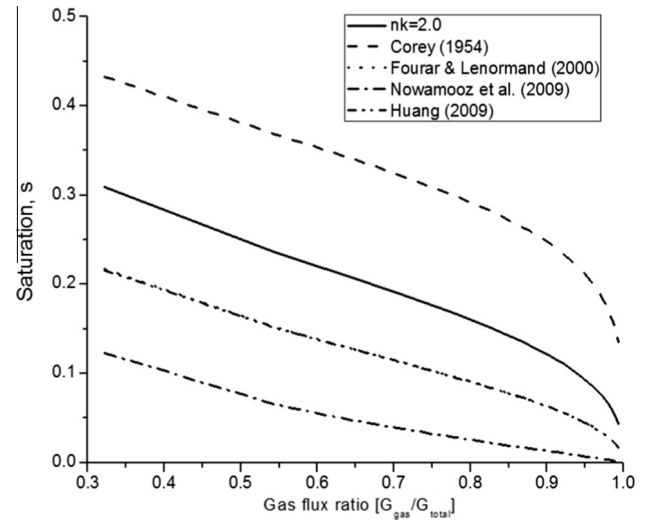


Fig. 6. Saturation level estimated by the two-fluid model ( $n_k$  is the exponent in Eq. (29)).

To compare model predictions with experimental data, the mean absolute error (MAE) was taken:

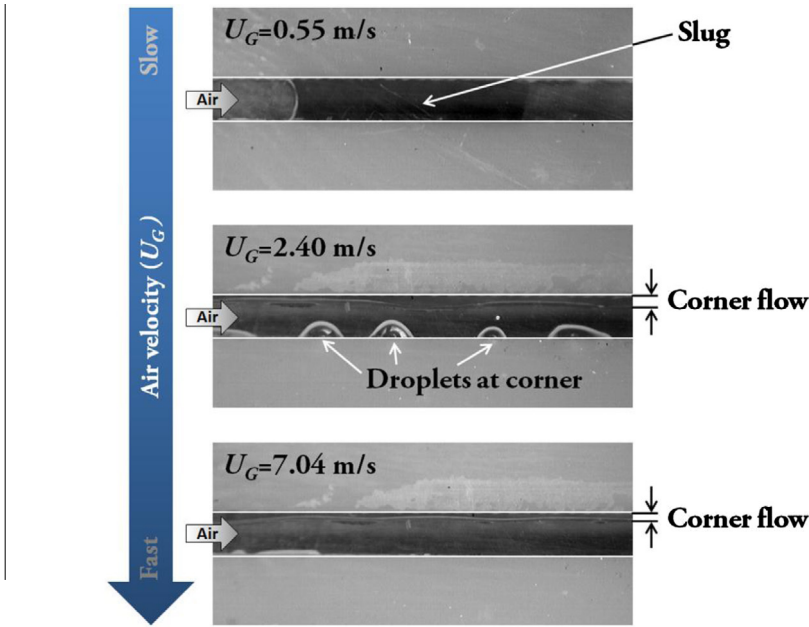
$$MAE = \frac{1}{N} \sum_N \left| \frac{[dp/dx]_{TP, predicted} - [dp/dx]_{TP, measured}}{[dp/dx]_{TP, measured}} \right| \times 100 [\%] \quad (37)$$

In addition, the liquid saturation  $s_l$  can be evaluated by the two-fluid model as well [30]. Fig. 6 presents the liquid saturation predicted by the two-fluid model using different correlations for the relative permeability. Liquid saturation changes inversely with the gas flow rate, because the gas flow provides the force to drive liquid flow. It can be seen that the choice of the relative permeability correlation significantly affects the prediction of liquid saturation.

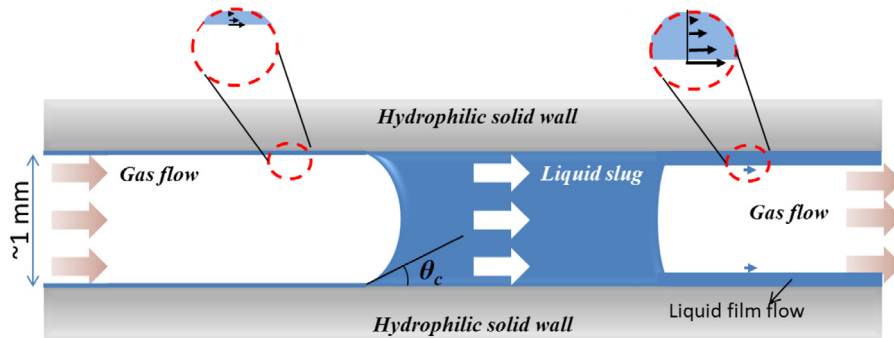
## 4. Results

### 4.1. Two-phase flow patterns

In experiments, three major patterns of two-phase flows were observed, as shown in Fig. 7. Under low gas flow rates (the top plot in Fig. 7(a)), liquid water cannot be efficiently removed by gas flow, thus accumulates and eventually block the channel by forming slug flow. Slug formation considerably increases pressure drop: when a slug forms, the liquid water in the slug rapidly accelerates to the speed of gas flow, i.e. the upstream gas flow needs to push the slug to move at the same pace as the gas flow. In addition, rapidly-moving slug constantly absorbs low-speed film liquid, resisting gas-phase flow, see Fig. 7(b). Note the liquid film flow is much slower than the gas flow. As the air flow rate increases (the middle plot in Fig. 7(a)), the drag force by air flow becomes larger, reducing liquid accumulation and eventually avoiding slug formation. As shown in the figure, liquid droplets under certain size appear in the corner areas. A droplet can remain static when the drag force by the air flow is relatively weak or move along with the gas flow when the gas flow drag overcomes the wall adhesion on the droplet. In certain condition, droplets merge, yielding a big bulk droplet as a result of surface tension to minimize the surface energy. In addition, liquid corner flow or film flow with wavy phase interface was also observed. Unstable flow, droplet formation (which influences local gas flow), or droplet merging to film flow may cause the wavy interface. In addition, as seen from this figure, topography of two-phase flow varies from location to location under this intermediate gas flow condition. Droplets can appear



(a) Visualization of two-phase flow patterns ( $U_L = 3.5 \times 10^{-4} \text{ m/s}$ ). The direction of the gravitational force is perpendicular to the images



(b) Schematic of slug formation in a micro-scale hydrophilic channel. The rapidly-moving slug absorbs low-speed film liquid, resisting gas-phase flow

Fig. 7. Visualization of two-phase flow patterns; and a schematic of slug formation.

in all or part of the corners. Liquid flow on the flat wall is difficult to see from this visualization; we suspect there will be some due to the hydrophilic surface. As the air flow rate further increases (the bottom plot in Fig. 7(a)), small droplets cannot remain static, and liquid water forms film flow on the surface with smooth liquid–air interface: the two-phase flow becomes stable stratified flow. In addition, similar flow patterns were observed in Adroher and Wang [30]. Different with their work, the present study considered a longer channel length, which has less impact from the outlet area: the two-phase flow in the outlet area shows complex dynamics as a result of the sudden change in flow path: from a narrow channel to a wide space of the outlet (manifold). They showed a figure (Fig. 8 in Ref. [27]) of highly unstable two-phase dynamics occurring in the outlet area, which likely affects the upstream flow.

4.2. Two-phase pressure drop

The flow pattern visualization indicates that the channel flow experiences differing two-phase flow structures and interaction, depending on flow conditions. Consequently, the pressure drop

can follow different trends. For annulus, analytical solutions can be derived for both tube and 2-D channel flows, see Fig. 8.

4.2.1. 2-D theoretical solution for annulus tube flow

Fig. 8 schematically sketches the two-phase annulus flow with a stable liquid–gas interface. In the following analysis, a uniform liquid film thickness is assumed, which is consistent with the experimental condition: in the experiment, liquid is injected

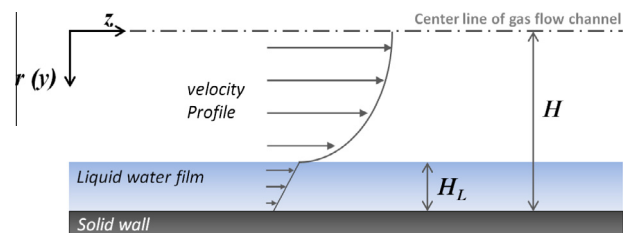


Fig. 8. Schematic of two-phase flow (annulus) in a 2-D channel (between two parallel plates) or tube in the analysis.

through an inlet port only, thus the liquid film after the port is uniform in its thickness (if it is stable annulus). In this considered flow pattern, the liquid velocity is much less than the gas one, because the film is usually thin and liquid viscosity is relatively large. For analysis purpose, we assume no-slip condition. This assumption enables us to obtain analytical solution based on existing pipe flow theories. Assuming fully developed condition for gas flow, the gas-flow momentum equation can be written by:

$$\frac{1}{r} \frac{\partial}{\partial r} \left( r \frac{\partial u}{\partial r} \right) - \frac{1}{\mu} \frac{dp}{dz} = 0 \quad (38)$$

The symmetry at the channel centerline and no-slip condition on the surface of liquid phase are set as the boundary conditions:

$$\begin{aligned} \frac{\partial u}{\partial r} &= 0 \quad @ \quad r = 0 \\ u &= 0 \quad @ \quad r = H - H_L \end{aligned} \quad (39)$$

Note that liquid film covers all the inner surface and the channel diameter is  $2H$ . The above problem is analytically solved to obtain the gas velocity:

$$u(r) = \frac{1}{4\mu} \frac{dp}{dz} [r^2 - (H - H_L)^2] \quad (40)$$

Integrating the gas-flow velocity to obtain the volumetric flux, the superficial gas velocity  $U_G$ , is calculated by:

$$U_G = \frac{1}{\pi H^2} \int_0^{H-H_L} u(r) \cdot 2\pi r dr = -\frac{1}{8\mu} \frac{dp}{dz} \frac{1}{H^2} (H - H_L)^4 \quad (41)$$

Through comparing with Darcy's law (Eq. (25)), the relative permeability is derived as:

$$k_{rg}K = \frac{1}{8H^2} (H - H_L)^4 = \frac{H^2}{8} \left( 1 - \frac{H_L}{H} \right)^4 \quad (42)$$

The liquid saturation in a cylindrical domain is defined as the ratio of the liquid volume to channel volume, i.e.

$$s_l = 2 \frac{H_L}{H} - \left( \frac{H_L}{H} \right)^2 \rightarrow 1 - s_l = \left( 1 - \frac{H_L}{H} \right)^2 \quad (43)$$

Eq. (42) then changes to:

$$k_{rg}K = \frac{H^2}{8} (1 - s_l)^2 \Rightarrow k_{rg} = A(1 - s_l)^2 \quad (44)$$

$A$  is a constant depending on the absolute permeability and channel geometry ( $A = H^2/8K$ ). In addition,  $k_{rg}$  equals to 1 when  $s_l = 0$ , thus  $A = 1$  or

$$k_{rg} = (1 - s_l)^2 \quad (45)$$

Compared to the relative permeability defined by Eq. (29), this derivation shows  $n_k$  is 2. Note that the above is for the annulus flow in a tube.

#### 4.2.2. Theoretical solution for flows between parallel plates

Similar steps are followed for analytic solution of laminar film flows between two parallel plates. In this case, liquid film covers the surface of both plates, and the channel height is  $2H$ . A stratified flow between two parallel infinite plates is assumed and 2-D momentum equation is expressed as:

$$\mu \frac{\partial^2 u}{\partial y^2} - \frac{dp}{dx} = 0 \quad (46)$$

Boundary conditions are based on the symmetric velocity profile and non-slip condition, and the fully developed velocity profile is solved as:

$$u(y) = \frac{1}{2\mu} \frac{dp}{dx} [y^2 - (H - H_L)^2] \quad (47)$$

The corresponding superficial air velocity is calculated by

$$u_g = -\frac{1}{3\mu} \frac{dp}{dx} \frac{1}{H} (H - H_L)^3 \quad (48)$$

In this situation, the liquid saturation is the ratio of channel height and water film thickness, i.e.

$$s_l = \frac{H_L}{H} \quad (49)$$

By comparing with Darcy's law, the permeability is expressed as a function of saturation:

$$k_{rg}K = \frac{H^2}{3} (1 - s_l)^3 \quad (50)$$

Compared to the relative permeability defined in Eq. (29), the above derivation indicates that  $n_k$  is equal to 3 for stratified flow between two parallel plates.

#### 4.2.3. Experimental results

Fig. 9 compares the present experimental data with the prediction of several empirical models using the Lockhart–Martinelli parameter. For the two conditions of low liquid flow rates, i.e. (a) and (b), all of the models agree reasonably well with the experimental data. For the two high liquid injection rates, i.e. (c) and (d), the predictions deviate from the experimental curve a little bit, but still follow the trend. The experimental results show a large fluctuation in the measurement. The fluctuation likely results from the fact that a higher addition rate of liquid causes more water accumulation, yielding unstable two-phase flow. The deviation becomes larger under higher liquid flow rates.

Fig. 10 shows the two-fluid model predictions using different correlations of relative permeability against the experimental data. Again, most of the correlations show a good match with the experimental data under low liquid flow rates. Under high liquid flow rates, good match was achieved by some correlations (e.g.,  $n_k = 2.0$  and 2.5). As to the fluctuation under high liquid injection rates, most of the experimental data are enclosed by the two lines of the relative permeability correlation (Eq. (29)) using  $n_k = 2.0$  and 2.5 except under the very low gas flow rate. Fig. 11 presents detailed comparison between the experimental measurement and model prediction for each correlation of the relative permeability. Most cases show a close match with experimental data in the regime of high air flow rate (or high pressure drop regime) except the ones from Corey; whereas they deviate to some degree in the regime of low air flow rate. In particular, Huang, Fourar, and Eq. (29) with  $n_k$  of 2.5 show a better match within <10% of the mean absolute error (MAE). In addition, when increasing  $n_k$ , the predicted pressure drop increases. This is because a higher  $n_k$  physically represents a larger effect of the liquid-phase presence on the gas-phase flow. Given that flow pattern determines two-phase interaction, the pressure drop can follow a specific trend for each flow pattern, in another word, one correlation of the relative permeability may fit in one or a few flow patterns, not all of them. A higher value of exponent  $n_k$  fits in a flow pattern where a larger impact of liquid presence on air flow is present, e.g. slug flow. A low value of  $n_k$  is corresponding to the condition of stable liquid film flow, where the two-phase interaction is relatively weak. Fig. 12 compares the model prediction using the set of determined exponents in Eq. (29) and the experimental data for different flow patterns. The flow pattern is determined through both flow visualization and measured pressure evolution. Adopting 2.49, 2.15 and 1.96 for  $n_k$  is found to be the best match with the experimental data, for slug, mixed and annulus flow, respectively. As the gas flow rate increases, i.e. the inertial force dominates the flow, the wetting phase of liquid becomes film and the exponent value is around 2.0, close to the analytic result for annulus in a tube.

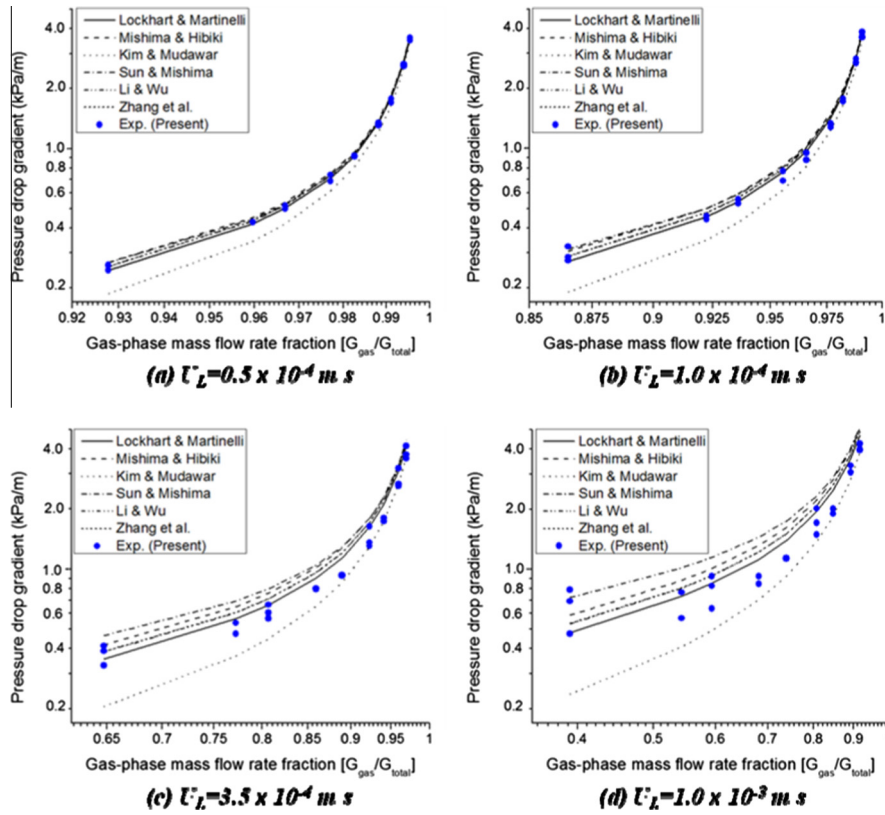


Fig. 9. Two-phase pressure drop measured by experiment and predicted by the Martinelli-parameter-based models.

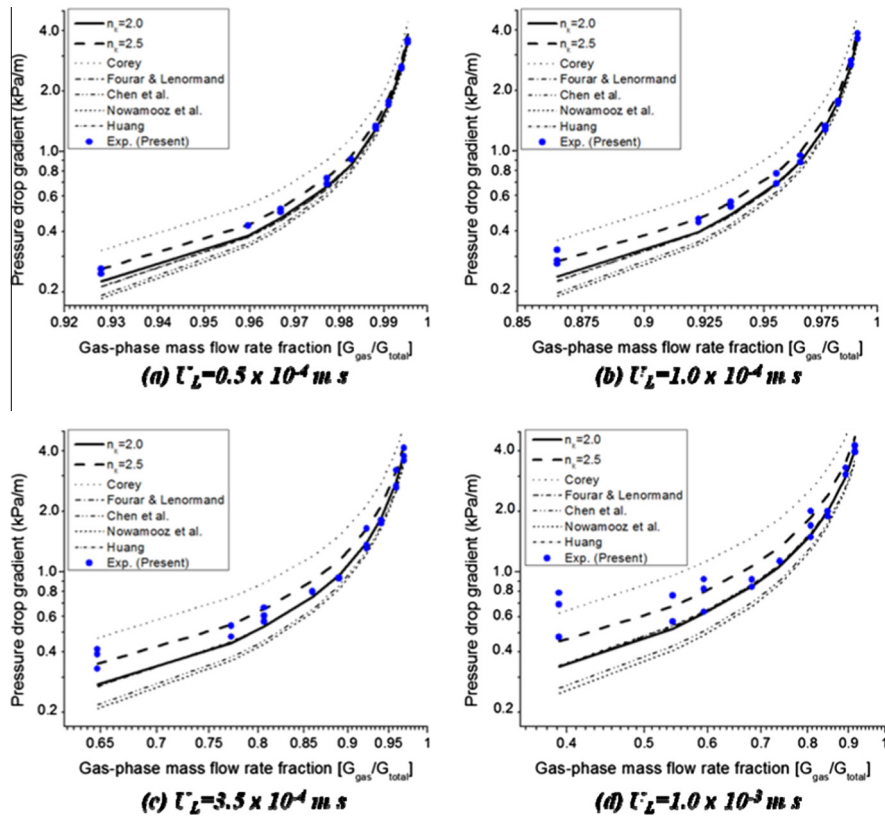


Fig. 10. Two-phase pressure drop measured by experiment and predicted by the two-fluid model.

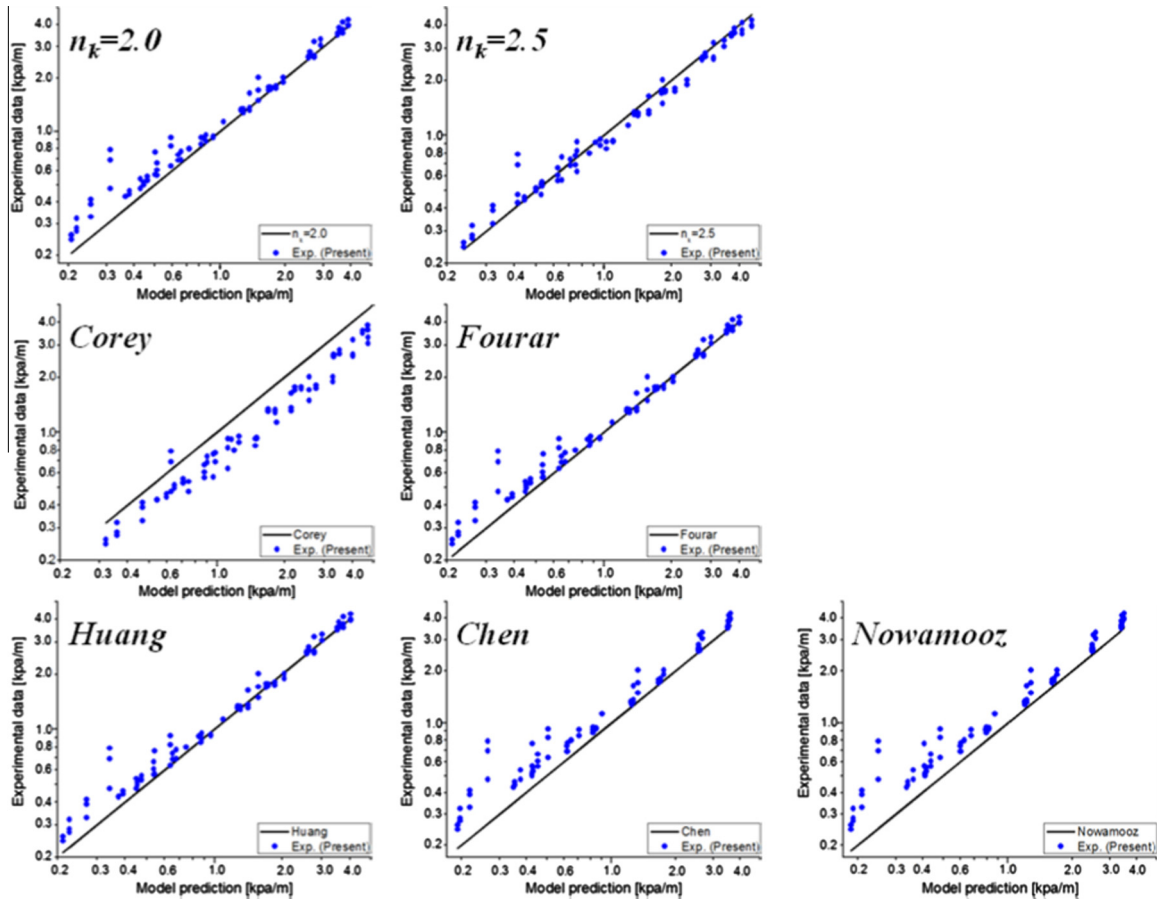


Fig. 11. Detailed comparisons between experimental data and model predictions on pressure drop using various relative permeability models.

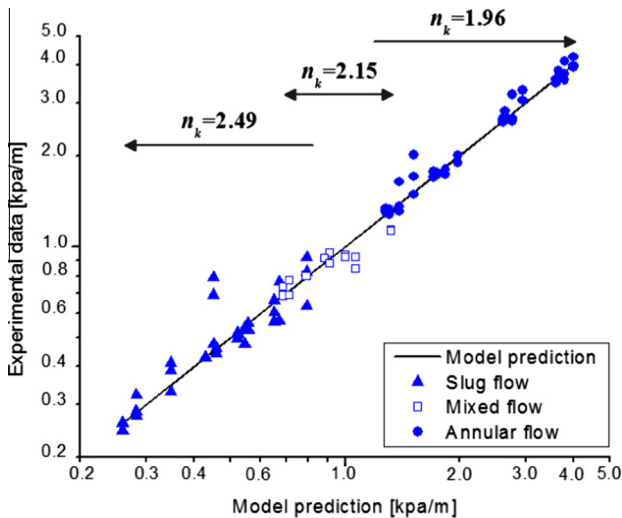


Fig. 12. Determined  $n_k$  values for each flow pattern.

The set of exponents are also bounded or almost bounded by the analytical results for the flows in a tube and two parallel plates (i.e.  $n_k = 2.0$  and  $3.0$ , respectively).

### 4.3. Two-phase multiplier

The two-phase friction multiplier is an important parameter, quantifying the effect of liquid presence on the gas-phase pressure

drop. Fig. 13 compares the experimental data with the empirical models using the Lockhart–Martinelli parameter. Under the conditions of high air flow and low liquid flow rates when two-phase flows are more stable, the gap among the model predictions is small, and the model prediction shows a good agreement with the experimental data. In the two cases of high liquid flow rates, most of the model predictions show acceptable agreement with the experimental data. In Fig. 14, the experimental data are compared to the predictions of the two-fluid model using various relative permeability correlations. As seen from the figure, the predictions vary considerably among the relative-permeability correlations. For higher gas-flow rates, the correlations of Huang et al. and Fourar and Lenormand predict the experimental trend well; under low air-flow regimes using Eq. (29) with a larger exponent value captures the trend better. The predictions using optimized  $n_k$  values are also plotted, showing a close match with the experimental data.

### 4.4. Two-phase flow pressure drop

In addition to the friction multiplier, real-time pressure provides detailed information regarding two-phase flow dynamics, which is presented in Fig. 15. Upon slug formation, pressure drop responds with a jump till the slug is removed out of the channel. As the slug is removed, the pressure rapidly returns to the previous low state. As a result, a spike appears in the pressure evolution which reflects the formation and removal of one slug. In a real case when slug forms constantly, the spike occurs periodically, corresponding to slug formation and removal under low air velocity ( $U_G < \sim 2$  m/s), as seen in Fig. 15. In addition, Tronconi [41]

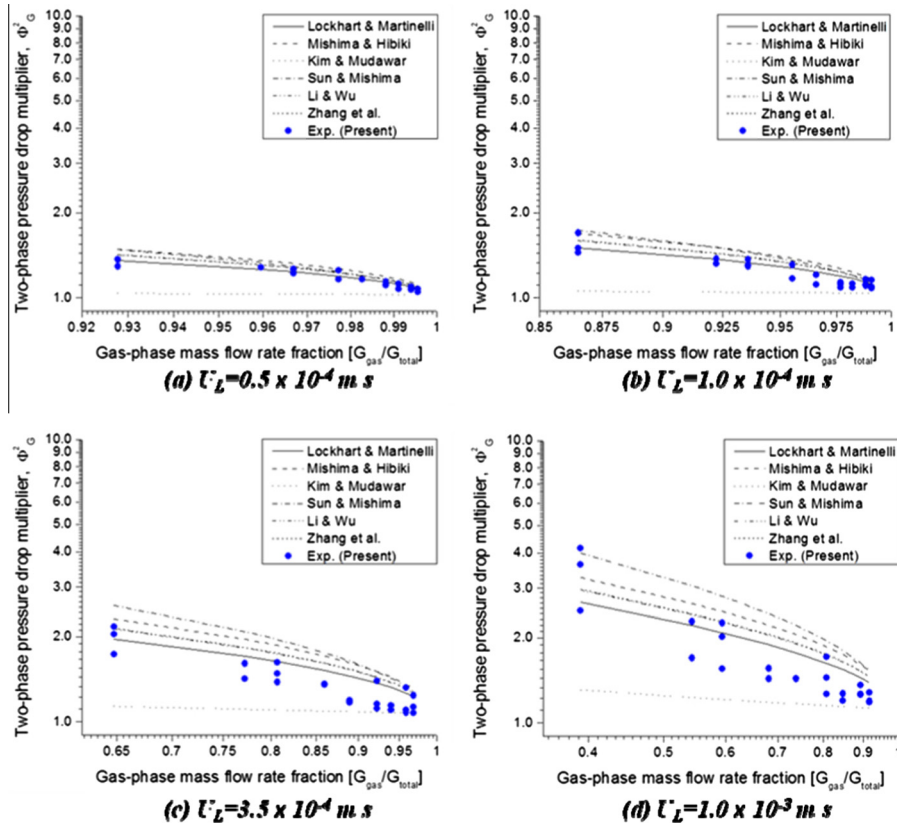


Fig. 13. Two-phase friction multiplier measured by experiment and predicted by the Martinelli-parameter-based models.

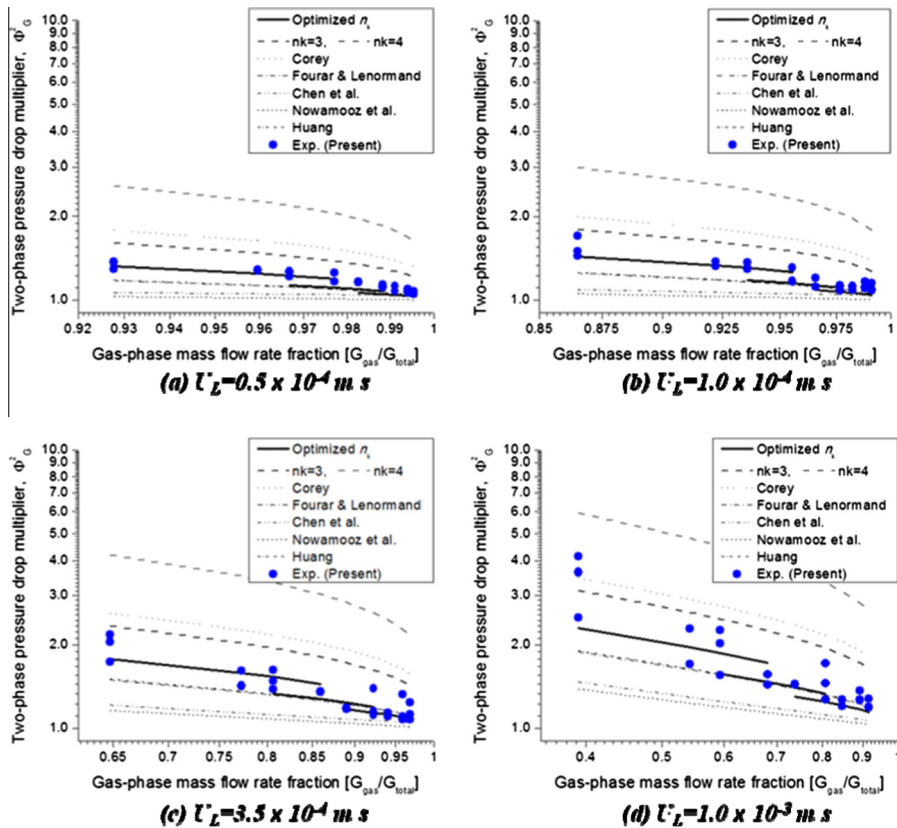


Fig. 14. Two-phase friction multiplier measured by experiment and predicted by the two-fluid model.

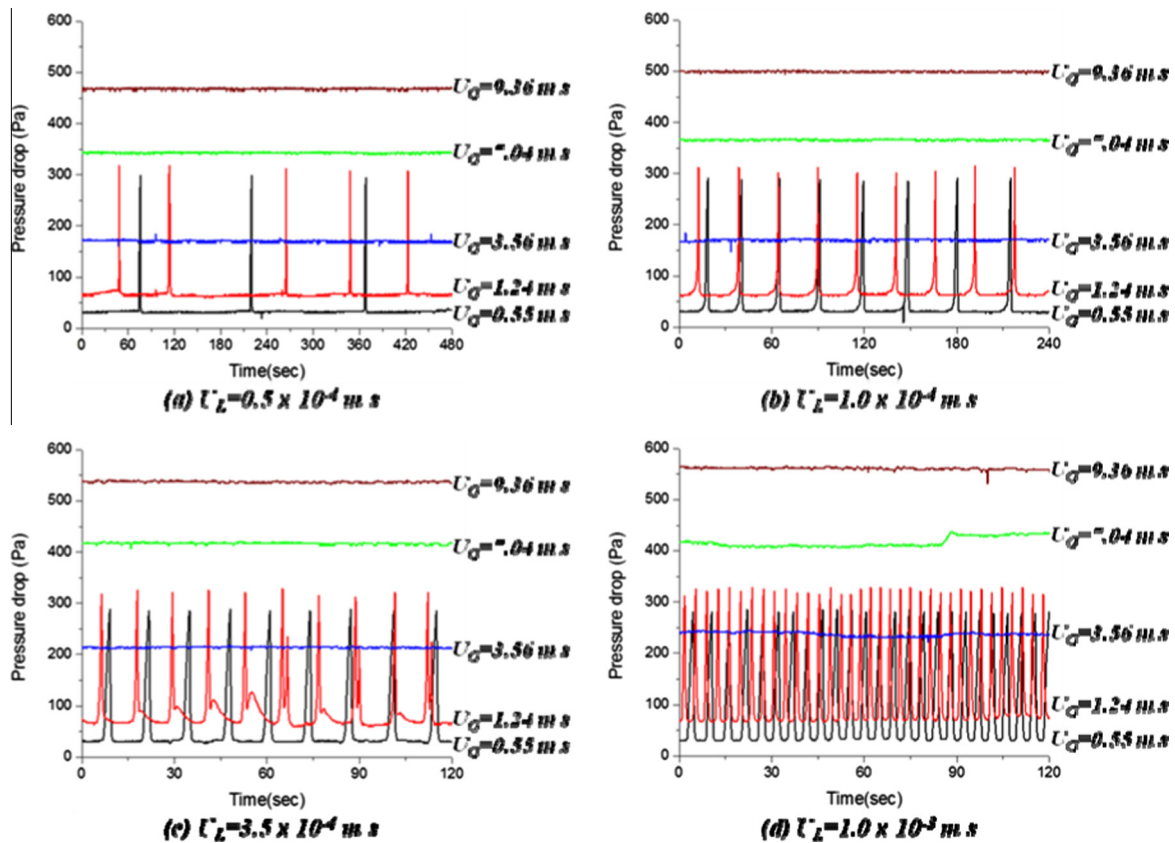


Fig. 15. Real-time pressures under various operating conditions.

experimentally showed that the frequency of slug formation exponentially increases with decreasing air flow rate. For the pattern between slug and annulus, e.g.  $U_G = 3.56$  m/s, the overall pressure drop becomes more stable with small fluctuation caused by wavy surface of corner flow or droplet formation/removal in the corner region. In annulus, which is stable and occurs at high air velocity, the pressure drop becomes stabilized without any significant spikes. From the measurement, the critical air velocity for stabilized flow (i.e. no pressure fluctuation) is about 2.0 m/s. Note that the value of critical velocity is determined by channel dimension, geometry, wall properties and fluid properties.

## 5. Conclusion

In this study, two-phase flows in a micro hydrophilic channel were studied experimentally, numerically, and analytically. Three main flow patterns were observed through visualization in the range of operating condition, they are slug flow, wavy, and annulus. Two sets of models were considered for numerical study: they are empirical models using the Lockhart–Martinelli parameter and a two-fluid model using various correlations of relative permeability. Prediction of both models showed an acceptable agreement with experimental data under low liquid flow rates, while deviates to some degree under high liquid rates. Under low gas and high liquid flow rates, flow can be unstable, causing considerable fluctuation in pressure drop. Using the power-relation correlation for the relative permeability to match with experimental data, the values of the exponent are found to be 2.49, 2.15 and 1.96 for slug, wavy, and annulus flow, respectively. 2-D analysis on film flows in a tube and 2D channel (two parallel plates) was performed, showing the derived  $n_k$  ranges 2.0–3.0. The real-time pressure was presented and showed flow pattern also affects pressure drop evolution;

and slug formation/removal leads to pressure spikes. The critical velocity  $U_c$  from stable flow with no pressure fluctuation to unstable flow was found to be  $\sim 2.0$  m/s.

## Acknowledgements

Technical support from RapidTech at the UC Irvine and partial financial support from Sandia National laboratories are gratefully acknowledged.

## References

- [1] S.V. Garimella, C.B. Sobhan, Transport in microchannels – A critical review, *Annu. Rev. Heat Transfer* 13 (2003) 1–50.
- [2] Y. Wang, S. Basu, C.Y. Wang, Modeling two-phase flow in PEM fuel cell channels, *J. Power Sources* 179 (2008) 603–617.
- [3] L.L. Vasiliev, Micro and miniature heat pipes – Electronic component coolers, *Appl. Therm. Eng.* 28 (4) (2008) 266–273.
- [4] Y. Han, Y. Liu, M. Li, J. Huang, A review of development of micro-channel heat exchanger applied in air-conditioning system, *Energy Procedia* 14 (2012) 148–153.
- [5] Z.Y. Guo, Z.X. Li, Size effect on single-phase channel flow transfer at microscale, *Int. J. Heat Fluid flow* 24 (3) (2003) 284–298.
- [6] X. Liu, H. Guo, F. Ye, C.F. Ma, Flow dynamic characteristics in flow field of proton exchange membrane fuel cells, *Int. J. Hydrogen Energy* 33 (2008) 1040–1051.
- [7] R. Anderson, L. Zhang, Y. Ding, M. Blanco, X. Bi, D.P. Wilkinson, A critical review of two-phase flow in gas flow channels of proton exchange membrane fuel cells, *J. Power Sources* 195 (15) (2010) 4531–4553.
- [8] H.P. Ma, H.M. Zhang, J. Hu, Y.H. Cai, B.L. Yi, Diagnostic tool to detect liquid water removal in the cathode channels of proton exchange membrane fuel cells, *J. Power Sources* 162 (2006) 469–473.
- [9] D. Spornjack, A.K. Prasad, S.G. Advani, Experimental investigation of liquid water formation and transport in a transparent single-serpentine PEM fuel cell, *J. Power Sources* 170 (2007) 334–344.
- [10] H. Masuda, K. Ito, T. Oshima, K. Sasaki, Visualisation of water droplets during the operation of PEM fuel cells, *J. Power Sources* 173 (2007) 137–148.

- [11] L. Cheng, G. Ribatski, J.R. Thome, Gas-liquid two-phase flow patterns and flow pattern maps: Fundamentals and applications, *Appl. Mech. Rev.* 61 (2008) 050802-1.
- [12] T.A. Trabold, Minichannels in polymer electrolyte membrane fuel cells, *Heat Transfer Eng.* 26 (2005) 3–12.
- [13] F.Y. Zhang, X.G. Yang, C.Y. Wang, Liquid water removal from a polymer electrolyte fuel cell, *J. Electrochem. Soc.* 153 (2006) A225–A232.
- [14] I.S. Hussaini, C.Y. Wang, Visualization and quantification of cathode channel flooding in PEM fuel cells, *J. Power Sources* 187 (2) (2009) 444–451.
- [15] R. Satija, D.L. Jacobson, M. Arif, S.A. Werner, In situ neutron imaging technique for evaluation of water management systems in operating PEM fuel cells, *J. Power Sources* 129 (2004) 238.
- [16] J. Zhang, K. Kramer, R. Shimoi, Y. Non, E. Lehmann, A. Wokaun, K. Shinohara, G. Scherer, In situ diagnostic of two-phase flow phenomena in polymer electrolyte fuel cells by neutron imaging: Part B. material variations, *Electrochim. Acta* 51 (2006) 2715.
- [17] J. Mishler, Y. Wang, P.P. Mukherjee, R. Mukundan, R.L. Borup, Subfreezing operation of polymer electrolyte fuel cells: Ice formation and cell performance loss, *Electrochim. Acta* 65 (2012) 127–133.
- [18] J. Mishler, Y. Wang, R. Mukundan, J. Spendelow, D.S. Hussey, D.L. Jacobson, R. Borup, Probing the water content in polymer electrolyte fuel cells using neutron radiography, *Electrochim. Acta* 75 (2012) 1–10.
- [19] M.P. David, J. Miler, J.E. Steinbrenner, Y. Yang, M. Touzelbaev, K.E. Goodson, Hydraulic and thermal characteristics of a vapor venting two-phase microchannel heat exchanger, *Int. J. Heat Mass Transfer* 54 (25–26) (2011) 5504–5516.
- [20] L. Zhang, E.N. Wang, K.E. Goodson, T.W. Kenny, Phase change phenomena in silicon microchannels, *Int. J. Heat Mass Transfer* 48 (8) (2005) 1572–1582.
- [21] H.Y. Wu, P. Cheng, Boiling instability in parallel silicon microchannels at different heat flux, *Int. J. Heat Mass Transfer* 47 (17–18) (2004) 3631–3641.
- [22] W.H. McAdams, W.K. Woods, L.C. Heroman, Vaporization inside horizontal tubes II—benzene-oil mixtures, *Trans. ASME* 64 (1942) 193–200.
- [23] A. Cicchitti, C. Lombardi, M. Silvestri, G. Soldaini, R. Zavalluilli, Two-phase cooling experiments pressure drop, heat transfer and burnout measurements, *Energia Nucleare* 7 (1960) 407–425.
- [24] R.W. Lockhart, R.C. Martinelli, Proposed correlation of data for isothermal two phase flow, two component flow in pipes, *Chem. Eng. Prog.* 45 (1949) 39–48.
- [25] K. Mishima, T. Hibiki, Some characteristics of air-water two-phase flow in small diameter vertical tubes, *Int. J. Multiphase Flow* 22 (1996) 703–712.
- [26] L. Sun, K. Mishima, Evaluation analysis of prediction methods for two-phase flow pressure drop in mini-channels, *Int. J. Multiphase Flow* 35 (2009) 47–54.
- [27] W. Li, Z. Wu, A general correlation for adiabatic two-phase pressure drop in micro/mini-channels, *Int. J. Heat Mass Transfer* 53 (2010) 2732–2739.
- [28] W. Zhang, T. Hibiki, K. Mishima, Correlations of two-phase frictional pressure drop and void fraction in mini-channel, *Int. J. Heat Mass Transfer* 53 (2010) 453–465.
- [29] S.M. Kim, I. Mudawar, Universal approach to predicting two-phase frictional pressure drop for adiabatic and condensing mini/micro-channel flows, *Int. J. Heat Mass Transfer* 55 (2012) 3246–3261.
- [30] Y. Wang, Analysis of channel two-phase flow, *J. Electrochem. Soc.* 156 (10) (2009) B1134–B1141.
- [31] X.C. Adroher, Y. Wang, Ex-situ and modeling study of two-phase flow in a single channel of polymer electrolyte membrane fuel cells, *J. Power Sources* 196 (2011) 9544–9551.
- [32] A. Nowamooz, G. Radilla, M. Fourar, Non-Darcian two-phase flow in a transparent replica of a rough-walled rock fracture, *Water Resour. Res.* 45 (2009) W07406.
- [33] M. Fourar, R. Lenormand, A viscous coupling model for relative permeabilities in fractures, Paper SPE 49006, in: *SPE Annual Technical Conference and Exhibition*, New Orleans, LA, 1998.
- [34] H. Huang, Z. Li, S. Liu, X.Y. Lu, Shan and chen type multiphase lattice boltzmann study of viscous coupling effects for two-phase flow in porous media, *Int. J. Numer. Methods Fluids* 61 (2009) 341–354.
- [35] C.Y. Chen, R.N. Horne, M. Fourar, Experimental study of liquid-gas flow structure effects on relative permeabilities in a fracture, *Water Resour. Res.* 40 (8) (2004) W08301.
- [36] R.R. Bittle, M.B. Pate, A theoretical model for predicting adiabatic capillary tube performance with alternative refrigerants, *ASH RAE Trans.* 102 (2) (1996) 52–64.
- [37] D.R.H. Beattie, P.B. Whalley, A simple two-phase frictional pressure drop calculation method, *Int. J. Multiphase Flow* 8 (1982) 83–87.
- [38] Y. Wang, C.Y. Wang, A non-isothermal, two-phase model for polymer electrolyte fuel cells, *J. Electrochem. Soc.* 153 (2006) A1193.
- [39] Y. Wang, C.Y. Wang, Two-phase transients of polymer electrolyte fuel cells, *J. Electrochem. Soc.* 154 (2007) B636.
- [40] A.T. Corey, The interrelation between gas and oil. Relative permeabilities, *Producers Mon.* 19 (1954) 38.
- [41] E. Tronconi, Prediction of slug frequency in horizontal two-phase slug flow, *AIChE J.* 36 (5) (1990) 701.